International Journal of Hydrogen Energy 97 (2025) 614–621

Contents lists available at ScienceDirect

International Journal of Hydrogen Energy

journal homepage: www.elsevier.com/locate/he

# Performance of industrial-scale solid oxide electrolysis cells: An assessment of leakage effects

E.V. Tsipis [a], A.V. Samoilov [a], D.V. Matveev [a], Yu.S. Fedotov [a], M.S. Dyakina [a], D.V. Zhigacheva [a], D.A. Agarkov [a,b,*], S.I. Bredikhin [a], V.V. Kharton [a]

[a] Osipyan Institute of Solid State Physics RAS, 2 Academician Osipyan str., Chernogolovka, Moscow District, 142432, Russia
[b] Moscow Institute of Physics and Technology, 9 Institutskiy per., Dolgoprudny, Moscow District, 141701, Russia

ARTICLE INFO

Handling Editor: Dr A Iranzo

*Keywords:*
Solid oxide electrolysis cell
Steam electrolysis
Hydrogen production
Life tests
Electrolyte degradation

ABSTRACT

Performance of one short-stack of the electrolyte-supported solid oxide electrolysis cells (SOECs) with multi-layered anodes based on $(Pr_{0.6}Sr_{0.4})_{0.97}MnO_{3-\delta}$ and cathodes made of Ni-based cermets was evaluated under the partial unhermetization conditions. Four industrial-scale 10×10 $cm^2$ membrane-electrode assemblies were produced, mounted in the stack, and tested for water vapor electrolysis at 1123 K in conditions when the sealant was partly cracked due to thermal cycling. The hydrogen production rate, faradaic efficiency and specific energy consumption determined as functions of the applied electrical current were compared with the same parameters for a hermetically sealed SOEC stack. The energy consumption for hydrogen generation was approximately 3 kWh/$Nm^3$. Appropriate operation regimes in the presence of sealant leakages may be achieved at maximum possible currents which are still lower than the current limit corresponding to the start of rapid SOEC degradation. The life tests performed at the current densities of ≥370 mA/$cm^2$ and subsequent microscopic studies showed that this degradation is associated with microstructural changes in the solid electrolyte ceramics. The air electrodes exhibited a high electrochemical activity both in the fuel-cell and electrolysis modes, without any indication of possible delamination from the solid electrolyte membranes.

## 1. Introduction

Use of hydrogen energy for electric power and heat generation is one of the most promising trends in the economic development, enabling to reduce carbon dioxide emissions [1–4]. Important challenges and limitations are associated, however, with carbon-free hydrogen production technologies. At present, approximately 48% hydrogen in the world is produced by the steam reforming of methane [5–7]. Other 30% and 18% are generated using oil reforming and coal gasification, respectively [5–7]. Water electrolysis is more friendly for the environment, but is only used for the production of less than 4% hydrogen up to now [5].

Solid oxide electrolysis cells (SOECs) are known as the most effective approach to the production of high-purity hydrogen due to the thermodynamic reasons originating from the high operating temperatures, typically in the range of 973–1173 [8–10]. For comparison, the energy consumption for commercially available proton-exchange membrane (PEM) electrolysis systems was estimated as 6.7 kWh/$Nm^3$ for Proton Onsite (USA) [11] and 4.8 kWh/$Nm^3$ for Enapter (Italy) [12]. For alkaline electrolysis cells, the energy consumption is close to 4.2–5.9 kWh/$Nm^3$ at the stack level and to 4.5–7.0 kWh/$Nm^3$ at the system level [13]. In the case of SOECs, the power-to-hydrogen efficiency may achieve the level up to >95% of $H_2$ heating value [14]. A biogas and biomethane processing plant comprising a combined electrolysis–methanation system using SOEC technology, with a capacity of 10 $Nm^3$/h, was operated for more than 2000 h and consumed approximately 3.07 kWh/$Nm^3$ for hydrogen production [15]. Similar consumption values were obtained for the plant with a capacity of 40 $Nm^3$/h [16]. The energy consumption of 3.09 kWh/$Nm^3$ was reported at the SOEC stack level at Haldor Topsøe [17]. In addition to the efficient hydrogen production, SOEC-based systems can also be used for the high-temperature $CO_2$ electrolysis [10,17].

The development of reliable SOEC technologies is essentially limited by materials science-related problems, in particular, irreversible degradation of the electrochemical cells due to the oxygen electrode (anode) delamination [18,19]. The delamination mechanism is often associated with an excess in local chemical potential of oxygen in the

* Corresponding author. Osipyan Institute of Solid State Physics RAS, Russian Academy of Sciences, 142432, Chernogolovka, Russia.
*E-mail address:* agarkov@issp.ac.ru (D.A. Agarkov).

https://doi.org/10.1016/j.ijhydene.2024.11.480
Received 16 September 2024; Received in revised form 20 November 2024; Accepted 29 November 2024
Available online 4 December 2024

solid electrolyte surface layers, leading to excessively high oxygen pressure at the anode/electrolyte interface. As an example, Fig. 1A shows one stage of stack disassembling for SOECs made of standard electrode materials, after testing in the steam electrolysis mode. After removing the membrane-electrode assembly (MEA), almost the entire anode layer based on lanthanum-strontium manganite (LSM) appears delaminated onto the bipolar plate, whilst the cathode layer remains unchanged on the electrolyte membrane. This problem may be solved by using an anode material with higher oxygen ionic conductivity and electrochemical activity, and/or by microstructural optimization of the anodes. Another reason for the SOEC degradation may refer to physical leakages in the stacks, which are typically sealed by glass-ceramic sealants. Such leakages lead to the oxidation of a part of hydrogen, thus lowering the energy conversion efficiency and inducing local heating.

Continuing our research in the field of solid oxide cells [20–23], this work was centered on appraisal of an alternative SOEC anode material based on $(Pr_{0.6}Sr_{0.4})_{0.97}MnO_{3-\delta}$ (PSM) and evaluation of the electrolyte-supported SOEC stack performance under the conditions of partial unhermitization.

## 2. Experimental

Single-phase powders of $(Pr_{0.6}Sr_{0.4})_{0.97}MnO_{3-\delta}$ (PSM), $(Pr_{0.8}Sr_{0.2})_{0.97}MnO_{3-\delta}$, $(La_{0.6}Sr_{0.4})_{0.97}MnO_{3-\delta}$ (LSM64) and $(La_{0.8}Sr_{0.2})_{0.95}MnO_{3-\delta}$ (LSM82) with perovskite-like structure were synthesized by the glycine-nitrate process with final annealing in air at 1273 K. All other powders were commercially available. Phase purity of all components was confirmed by the X-ray diffraction (XRD) analysis using a Rigaku SmartLab SE instrument ($CuK_\alpha$ radiation). In order to prepare inks for screen printing, pure or composite powders were ball-milled in an ethanol medium with the addition of 1 wt% 1,2-diaminopropane as a surfactant to prevent particle agglomeration, and then mixed with a binder V-006A and solvent RV372 (Heraeus, Germany). To produce dense ceramic samples for electrical conductivity measurements, the manganite powders were uniaxially pressed (60 MPa) and sintered in air at 1673 K for 5 h. The density of manganite ceramics was >97% of the theoretical values calculated from the XRD data. The total electrical conductivity was measured by four-probe DC technique in air.

The SOEC half-cells employed for the three-electrode measurements were produced with 0.1 cm thick membranes of 10 mol. % $Sc_2O_3$ and 1 mol. % $Y_2O_3$ co-stabilized $ZrO_2$ (10Sc1YSZ) solid electrolyte. Electrode layers in the form of a semicircle (geometric area of 1.2 $cm^2$) were screen-printed onto the electrolyte surface. In order to prevent chemical interaction between the electrode and electrolyte materials, a protective sublayer of $Ce_{0.9}Gd_{0.1}O_{1.95}$ (GDC10) was first applied. The working electrode (WE) consisted successively of a GDC10 sublayer, a functional layer of PSM - GDC10 (60-40 wt%) composite, and a current-collecting layer of LSM64. After screen-printing with intermediate drying steps, the multilayered WEs were sintered at 1473 K for 2 h in air. Fig. 2A illustrates the microstructure of as-sintered electrode layers. The Pt counter electrode (CE) and reference electrode (RE) were applied using platinum paste and annealed in air at 1223 K for 30 min. The CE was symmetrical to the WE; the RE with a diameter of ~0.1 cm was applied at a distance of at least 0.6 cm from the WE. This cell configuration was chosen to minimize errors in the electrode overpotential ($\eta$) determination [24–26]. The dependencies of $\eta$ on current density ($i$) were measured by the standard three-electrode technique in potentiostatic mode using an Autolab 302 N PGStat instrument equipped with a FRA32 module (Metrohm Autolab, Netherlands), at 1123 K. The relaxation time after changing the WE potential was 60 min. The values of ohmic and polarization resistances were extracted from the impedance spectra collected in the frequency range from 1 MHz down to 0.1 Hz, as

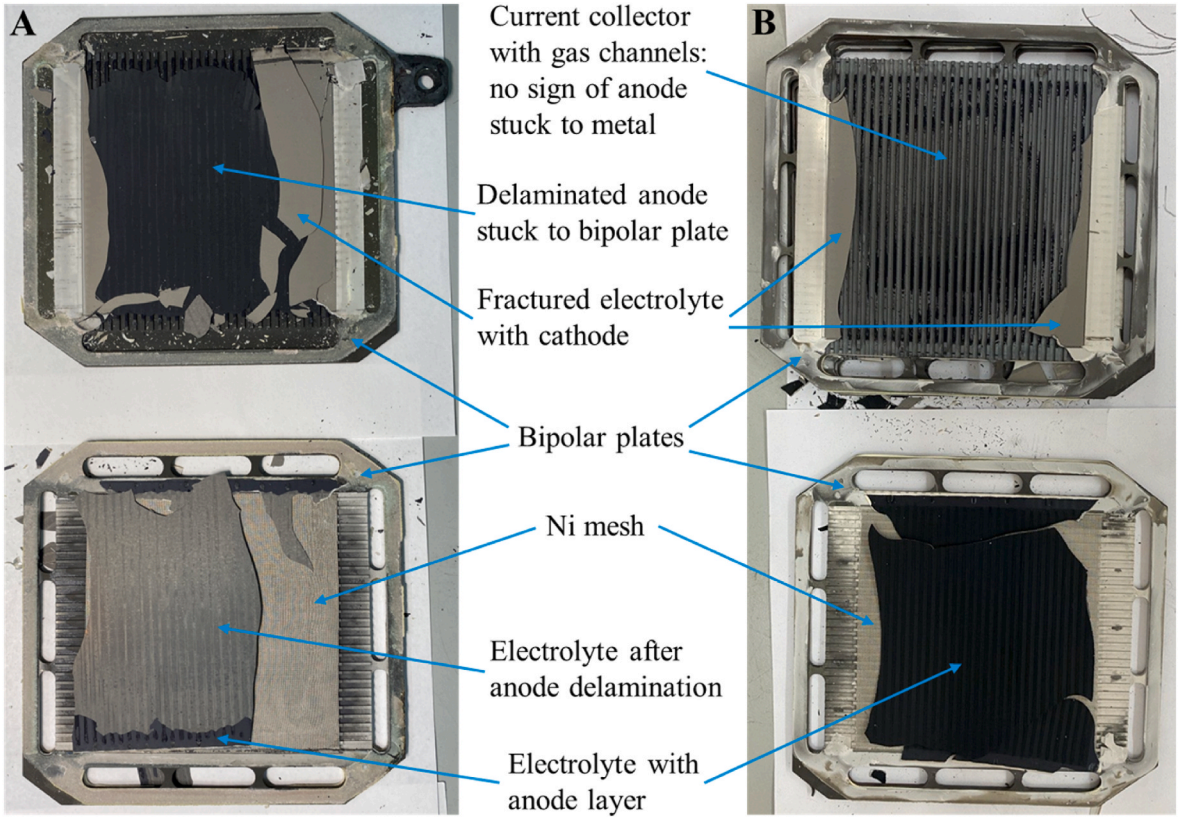


**Fig. 1.** Photographs showing one stage of SOEC stack disassembling after testing in the steam electrolysis mode: anodes with $(La_{0.8}Sr_{0.2})_{0.95}MnO_{3-\delta}$ - GDC10 composite (A), and $(Pr_{0.6}Sr_{0.4})_{0.95}MnO_{3-\delta}$ - GDC10 composite (B).

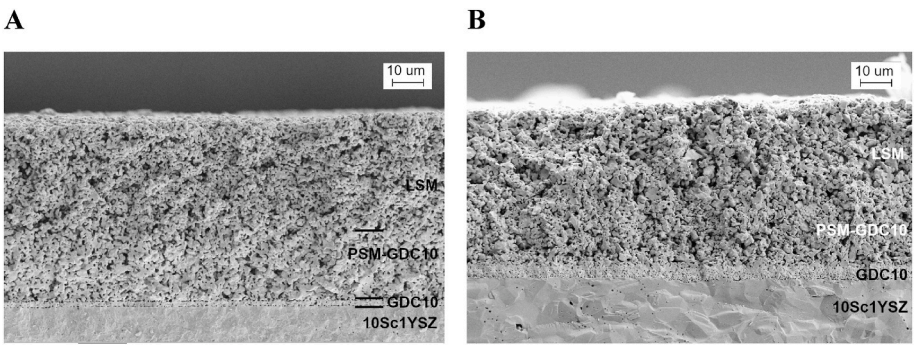


**Fig. 2.** SEM micrographs showing the working electrode fractures before (A) and after (B) electrochemical testing of the button cells.

illustrated in the inset of Fig. 3.

In order to produce the industrial-scale MEAs, dense three-layer membranes of 6 mol.% $Sc_2O_3$-stabilized $ZrO_2$ (6ScSZ)/10Sc1YSZ/6ScSZ (NEVZ-Ceramics, Russia) with 10 × 10 $cm^2$ size and thickness of 150 μm were used. The anodes consisted of GDC10, PSM - GDC10 (60-40 wt%) and LSM64, as for the half-cells. The cathodes comprised one protective GDC10 sublayer, a functional layer of NiO - GDC10 (50-50 wt %), a current-collecting layer of NiO - 10Sc1YSZ (60-40 wt%), and a contact layer of NiO. In order to improve sinterability, 2 mol.% CoO was added to the GDC10 and 10Sc1YSZ powders used for the functional and current-collecting cathode layers. The electrode layers (working surface of 9 × 9 $cm^2$) were deposited by screen-printing on an EKRA E2 instrument (EKRA Innovative Technologien, Germany) using meshes with thread densities from 24 up to 90 pcs/cm, and then co-sintered in air at 1473 K for 2 h. The microstructural features of the cells, as-prepared and after testing, were studied by the scanning electron microscopy (SEM, Supra 50-VP, CarlZeiss, Germany). The sintered electrode layers possess a homogeneous microstructure with submicron-sized grains and sufficient porosity (Fig. 4).

The fabricated four MEAs were assembled in a short stack. The bipolar interconnectors and end current collector plates were made of Crofer 22 APU steel (ThyssenKrupp, VDM Metals, Germany) by laser cutting and machining with subsequent galvanic deposition of

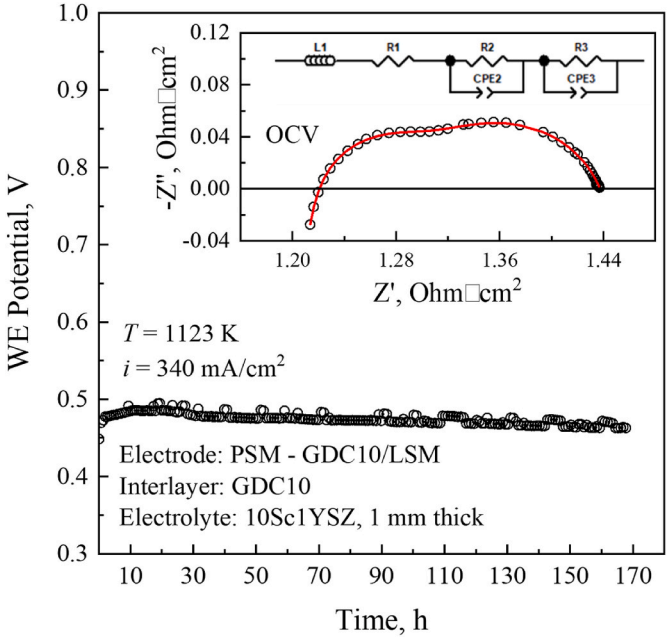


**Fig. 3.** Time dependence of the working electrode potential vs. RE at the constant anodic current density of 340 mA/$cm^2$ and 1123 K. Inset shows one example of the impedance spectra under OCV conditions, and an equivalent circuit used for the analysis.

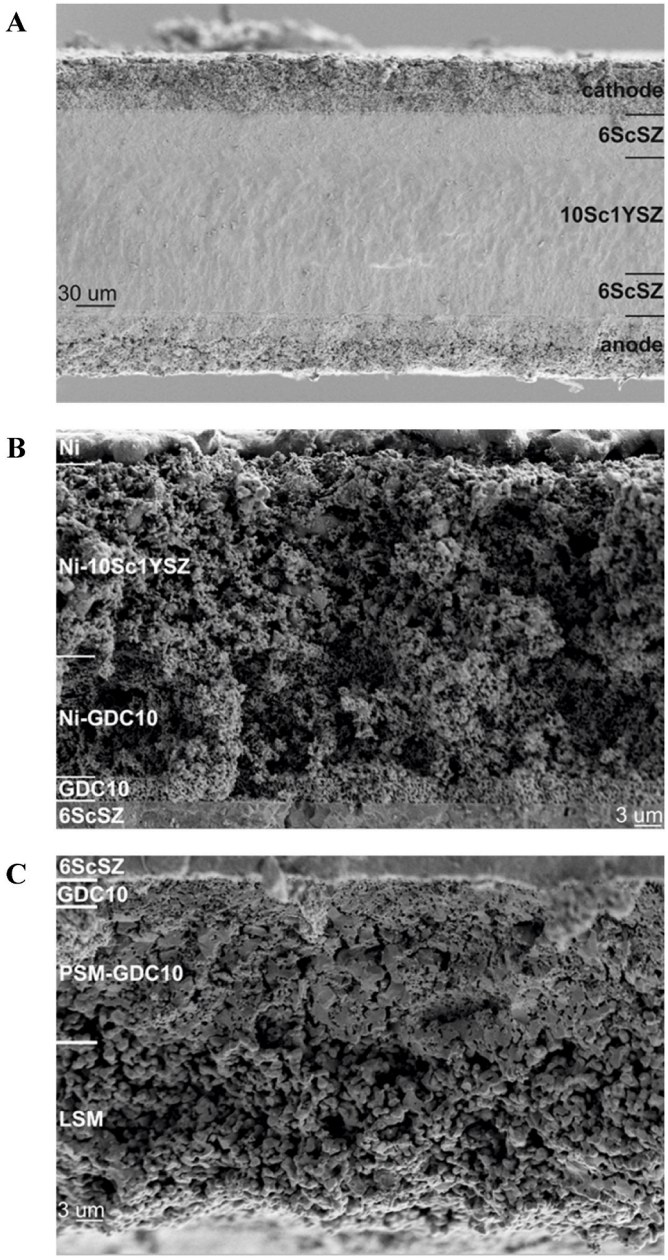


**Fig. 4.** SEM images showing cross-sections of a fractured single SOEC after testing: general view (A), cathode side (B) and anode side (C).

conductive protective Ni coatings. LSM82 was used to provide electrical contact between the ceramic anode and metal connectors. A ST02 high-temperature glass-ceramic sealant (Kerafol, Germany) was applied for the cell hermetization. Then all structural elements were assembled into an electrolysis unit, placed in the experimental setup described below, heated up to 1203 K (2 K/min) and sealed for 2 h. In order to simulate emergency shutdown leading to sealant cracking and partial unhermetization, the stack under air/$H_2$–$H_2O$ gradient was subjected to thermal cycling between 1123 and 873 K by switching off and turning on the setup furnace. After 3 cycles, the open circuit voltage (OCV) indicated an appearance of moderate leakage. Then the stack was tested in the steam electrolysis regime at 1123 K and disassembled. Subsequent microscopic analysis confirmed the formation of sealant cracks. Another short stack used as a reference, was made under identical conditions, sealed at 1203 K and tested at 1123 K without thermal cycling.

## 3. Results and discussion

### 3.1. Selection of the anode material

Despite the moderately lower electrical conductivity of $(Pr_{1-x}Sr_x)_{0.97}MnO_{3-\delta}$ with respect to lanthanum-strontium manganites (Fig. 5), the presence of catalytically active $Pr^{4+/3+}$ redox pair was expected to improve the anode performance. The compositions with higher strontium concentrations (PSM and LSM64) exhibit higher conductivity levels (Fig. 5) and were hence selected for functional and current-collecting layers of the SOEC anodes, respectively.

Fig. 6 displays the cathodic and anodic polarization curves of porous PSM-based electrodes, collected using the 3-electrode button cells at 1123 K in air. This method makes it possible to accurately measure overpotentials of individual WEs, thus providing direct information on their electrochemical activity [24–26]. The absolute values of the anodic overpotentials are slightly higher with respect to cathodic, which is indicative of modest differences in the oxygen reduction and evolution kinetics. Whatever the microscopic mechanisms of electrode reactions, the electrochemical activity of PSM-based electrode layers is quite high. For instance, at the anodic current density of 324 mA/cm$^2$, the electrode overpotential was 64 mV and electrode polarization resistance was 0.18 Ohm/cm$^2$.

The stability tests (Fig. 3) were carried out for 170 h under external anodic polarization. The current density selected for these tests

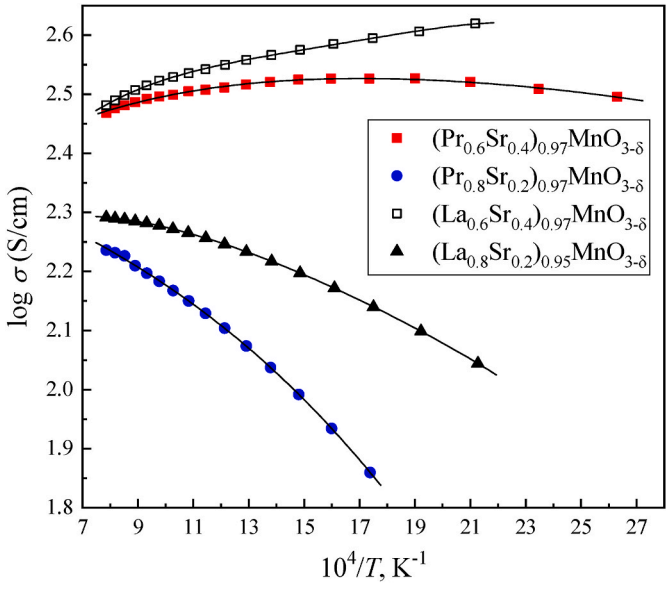


**Fig. 5.** Temperature dependencies of the total electrical conductivity of $(Pr_{1-x}Sr_x)_{0.97}MnO_{3-\delta}$ and $(La_{1-x}Sr_x)_{1-y}MnO_{3-\delta}$ ceramics in air.

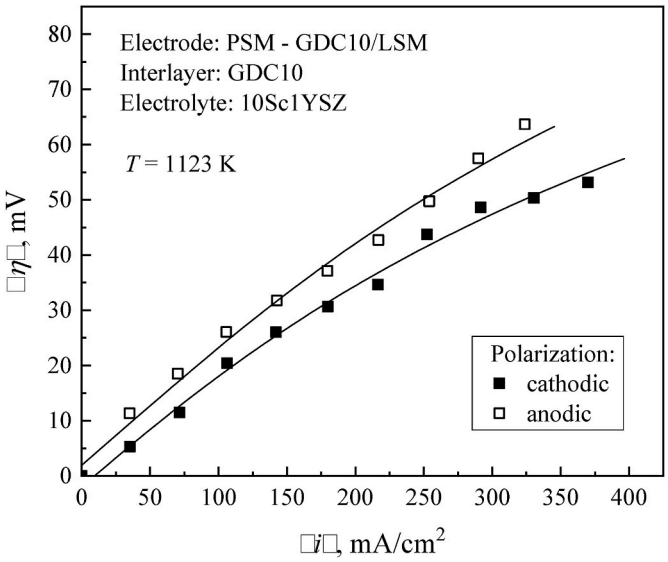


**Fig. 6.** Dependences of the cathodic and anodic overpotentials of porous PSM - GDC10/LSM64 electrode on the current density at 1123 K in air.

corresponds to the current of 28 A across a 10 × 10 cm$^2$ MEA (Fig. 3). No degradation was detected. Also, no microstructural changes were observed by subsequent SEM analysis (Fig. 2). Therefore, $(Pr_{0.6}Sr_{0.4})_{0.97}MnO_{3-\delta}$ was used to produce the large MEAs for further testing.

### 3.2. Experimental setup for hydrogen generation

Fig. 7 displays schematic drawing of the experimental setup, constructed and assembled for testing of the SOEC stacks. Each stack was placed in a high-temperature furnace where a protective gas (mixture of $H_2$ and Ar) was supplied into cathode chamber during heating and cooling of the unit in order to prevent cathode oxidation. After achieving the operation temperature, the fluxes of steam (10 Nl/min) and hydrogen (1.2 Nl/min) were supplied into the cathode chamber; the anode was exposed to flowing air (5 Nl/min). The current was applied using a SP-50 instrument equipped with FlexP 0160 booster (Biologic, France). The generated hydrogen was then dried in the drying unit and passed into the metal hydride modules (Research Center for Problems of Chemical Physics and Medicinal Chemistry RAS, Russia). Under external cooling, these modules absorb hydrogen; subsequent heating leads to its release at the total pressures up to 1.3 bar. Following the receiver, separated $H_2$ is then pumped into the cylinders using a hydrogen compressor (COVINT, Russia).

### 3.3. Leakage effect on the stack performance

Fig. 8 presents the voltage vs. current (*U–I*) curves of the short stack of four SOECs after thermal cycling. These dependencies are almost linear, suggesting the possibility for operation in a wide range of the applied currents. The direct current range from 10 up to 28 A was tested in this work. One should separately note that the supply of influent dry hydrogen was controlled by a carrier-gas flow regulator. The effluent gas flow rate was measured after the drying unit. As the inlet and outlet flow rates were measured for the dry gas, the total increase in the gas flux corresponds to hydrogen produced by the SOECs. The hydrogen generation rate ($V_{H2}$) can be calculated as

$$V_{H2} = Q_i - Q_0, \quad (1)$$

where $Q_i$ is the volume flow at a given current load, and $Q_0$ is the volume flow under OCV conditions. The specific energy consumption ($\Delta P$) for

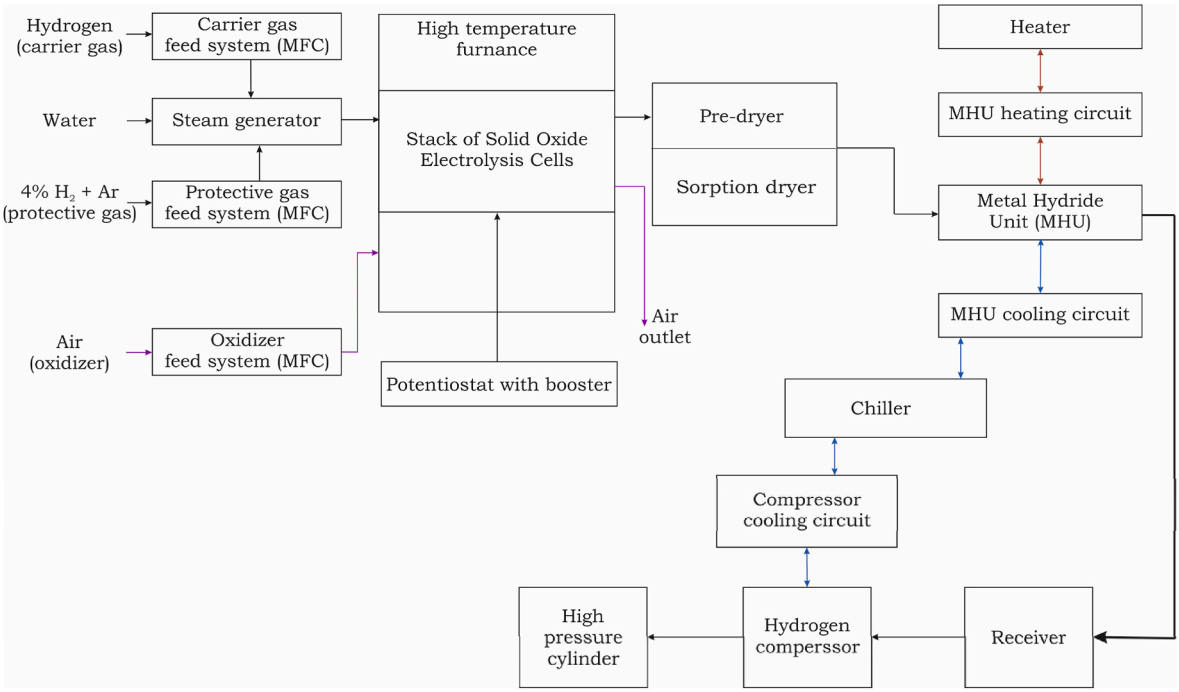


**Fig. 7.** Schematic drawing of the experimental setup for hydrogen generation. MFC is the system of mass-flow controllers.

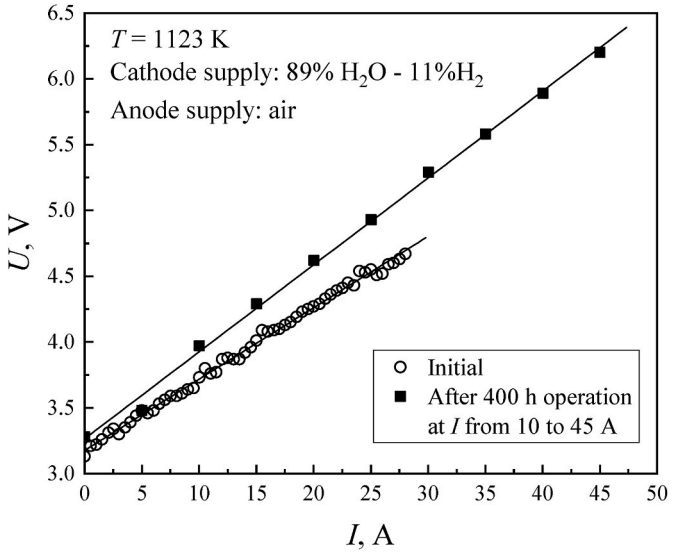


**Fig. 8.** Voltage vs. current dependencies for the SOEC short stack in flowing 89%$H_2O$ - 11%$H_2$ gas mixture at 1123 K before and after 400 h testing under current loads.

hydrogen production can be found as

$$\Delta P = \frac{U \bullet I}{V_{H2}} \quad (2)$$

In other words, the specific energy consumption can be directly calculated from three experimentally determined quantities, namely voltage, current and hydrogen generation rate. Table 1 lists their values and calculation results.

An important parameter of any electrolysis process is the faradaic efficiency ($\Phi$), the ratio between the experimental production rate and its theoretical value obtained from Faraday's law ($V_F$):

**Table 1**
Hydrogen production rates, faradaic efficiency and energy consumption for hydrogen generation in the unhermetized and hermetically sealed SOEC stacks.

| System with physical leakages | | | | | Hermetic reference system | |
|---|---|---|---|---|---|---|
| $I$, A | $U$, V | $V_{H2}$, Nml/min | $\Phi$, % | $\Delta P$, kWh/Nm$^3$ | $\Phi$, % | $\Delta P$, kWh/Nm$^3$ |
| 10 | 3.8 | 141.7 | 50.8 | 4.5 | 99.9 | 3.5 |
| 15 | 4.1 | 283.3 | 67.7 | 3.6 | 99.9 | 3.7 |
| 20 | 4.3 | 425.0 | 76.2 | 3.4 | | |
| 25 | 4.6 | 566.7 | 81.2 | 3.4 | | |
| 28 | 4.7 | 716.7 | 91.7 | 3.1 | | |
| 30 | 5 | 801.9 | 95.8 | 3.1 | | |
| 35 | 5.5 | 939.4 | 96.2 | 3.4 | | |
| 40 | 5.7 | 1082.5 | 97.0 | 3.5 | | |
| 45 | 6.1 | 1205.3 | 96.0 | 3.8 | | |

$$\Phi = \frac{V_{H2}}{V_F} \quad (3)$$

where

$$V_F = \frac{Mr \bullet I}{n \bullet F \bullet \rho} \quad (4)$$

$Mr$ is the molar mass of hydrogen, $n$ is the number of electrons, $F$ is the Faraday constant, and $\rho$ is the hydrogen density under normal conditions.

The obtained results are presented in Table 1. Although the OCV values (Fig. 8) are quite close to the theoretical estimate, the faradaic efficiency at 10 A is lower than 60%, unambiguously confirming leakages in the system. However, $\Phi$ tends to continuously increase with increasing current density. At the currents of ≥28 A, the faradaic efficiency reaches >90%, whilst the energy consumption stabilizes at the level of 3.1 kWh/Nm$^3$. Similar levels were obtained at 10–15 A for the reference stack hermetically sealed at the start, which was not subjected to thermal cycling. Although it seems quite logical that the leakage impact should decrease when the hydrogen generation rate increases, the obtained results demonstrate that SOECs may still be used for

hydrogen production even in the case of partial unhermetization, provided that the current density is sufficiently high. However, excessively high current densities may induce faster degradation of the cells, reflected by increasing energy consumption at the currents higher than 30 A (Table 1).

### 3.4. Performance degradation at high current densities

Short-term stability testing of the SOEC stack with partial unhermetization were carried out at the applied currents of 10, 30, 35 and 40 A (Fig. 9). Definite degradation in the stack performance was revealed in these conditions. Its rate was clearly dependent on the applied current and humidity. For instance, under the current load of 10 A, the voltage increased by 2% during 100 h, excluding the initial few hours when the voltage was unstable (Fig. 9A). Under the load of 30 A, the degradation rate was 10% per 100 h (Fig. 9B). A similar degradation rate was observed at the current load of 40 A. On the other hand, the current *vs.* voltage dependence remains linear (Fig. 8). Examples of the impedance spectra before and after the SOEC operation for 100 h (Fig. 9A) are displayed in Fig. 10. These spectra consist of three separable signals. The high-frequency contribution corresponds to the charge-transfer processes mainly at the anode; the intermediate-frequency and low-frequency arcs are associated with diffusion and gas-conversion impedance, respectively [27,28]. According to the impedance spectroscopy data, the degradation in SOEC performance is accompanied by

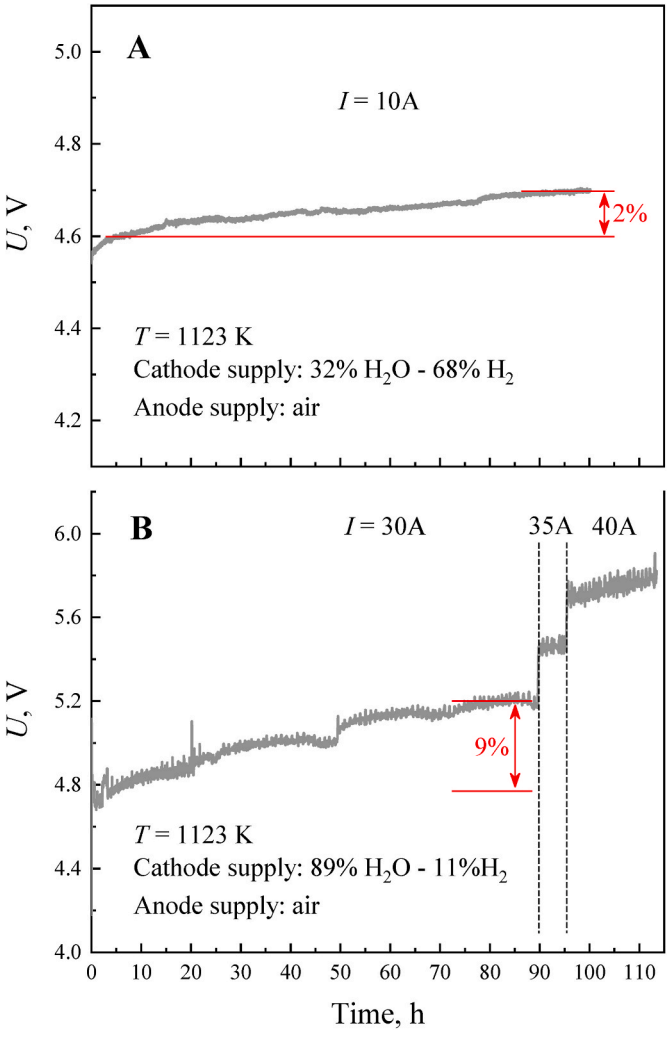


**Fig. 9.** Time dependencies of the SOEC stack voltage at constant direct currents of 10 A (A) and 30 A, 35 A and 40 A (B).

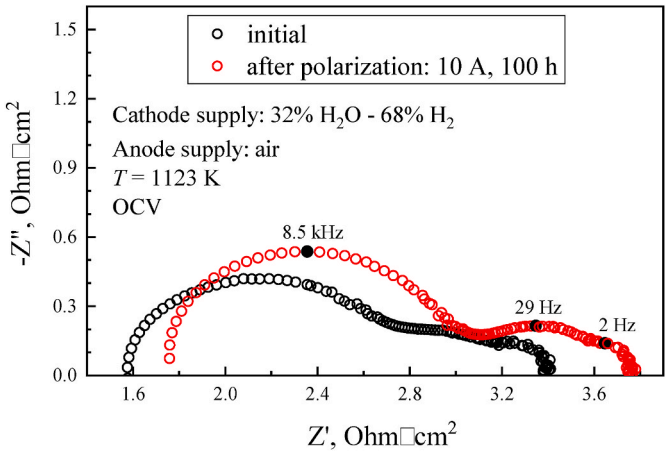


**Fig. 10.** Impedance spectra of the SOEC stack before and after the stability test at 10 A, illustrated in Fig. 9A.

increasing both ohmic and charge-transfer resistances. Taking into account the stable behavior of similar anode in the button cells (Fig. 3) and an increase in the degradation rate at high humidities (Fig. 9), increasing high-frequency contribution to the total electrode resistance may result from the partial oxidation of Ni-containing cathodes at high water vapor pressures. This factor may also contribute to the ohmic losses. Most likely, however, the increase in the ohmic resistance occurs due to microstructural changes in the solid electrolyte ceramics as discussed below.

SEM analysis of a fractured MEA after testing in the steam electrolysis mode for approximately 330 h under the current loads of 10–45 A, reveals faceting in the solid electrolyte ceramics in the vicinity of anode/electrolyte interface (Fig. 11A). Also, numerous nanopores formed at the grain facets and interfaces are observed (Fig. 11B and C). Similar phenomena were often reported [27–29] for the SOECs operating under high current densities and electrode overpotentials above 200 mV. These may originate from oxygen evolution at the grain boundaries forming pores and intergranular cracks [29–31]. Notice that this process may only be possible when electronic conduction was induced in zirconia ceramics. As a result of the microstructural changes, both the electrical resistance and fragility of the solid electrolyte membrane tend to progressively increase. The latter effect may even finally lead to the cell fracture. The literature data [30–32] suggest that the pore formation processes may be accompanied by cation migration. At the same time, no significant microstructural changes were observed for the electrodes. Moreover, no anode delamination was found upon stack disassembling (Fig. 1B, 4A and 4C). An opposite behavior was observed for the stack of MEAs with LSM82-based anode (Fig. 1A) where the air electrode delamination was responsible for the SOEC failure.

In summary, when the SOEC performance is affected by physical leakages, the current density should be maximum to improve the hydrogen production efficiency and to reduce the corresponding energy consumption. However, the current should not exceed a critical level where microstructural degradation of the solid electrolyte starts. Under experimental conditions used in the present study, this level was approximately 370 mA/cm$^2$.

## 4. Conclusions

Perovskite-type $(Pr_{0.6}Sr_{0.4})_{0.97}MnO_{3-\delta}$ was proposed as alternative anode material of the solid oxide electrolysis cells. The electrochemical activity of PSM-based air electrode was sufficiently high and stable under both cathodic and anodic polarization. At 1123 K and anodic current density of 324 mA/cm$^2$, the electrode overpotential was 64 mV and the electrode polarization resistance was 0.18 Ohm/cm$^2$. The industrial-scale electrolyte-supported SOECs with the size of 10 × 10

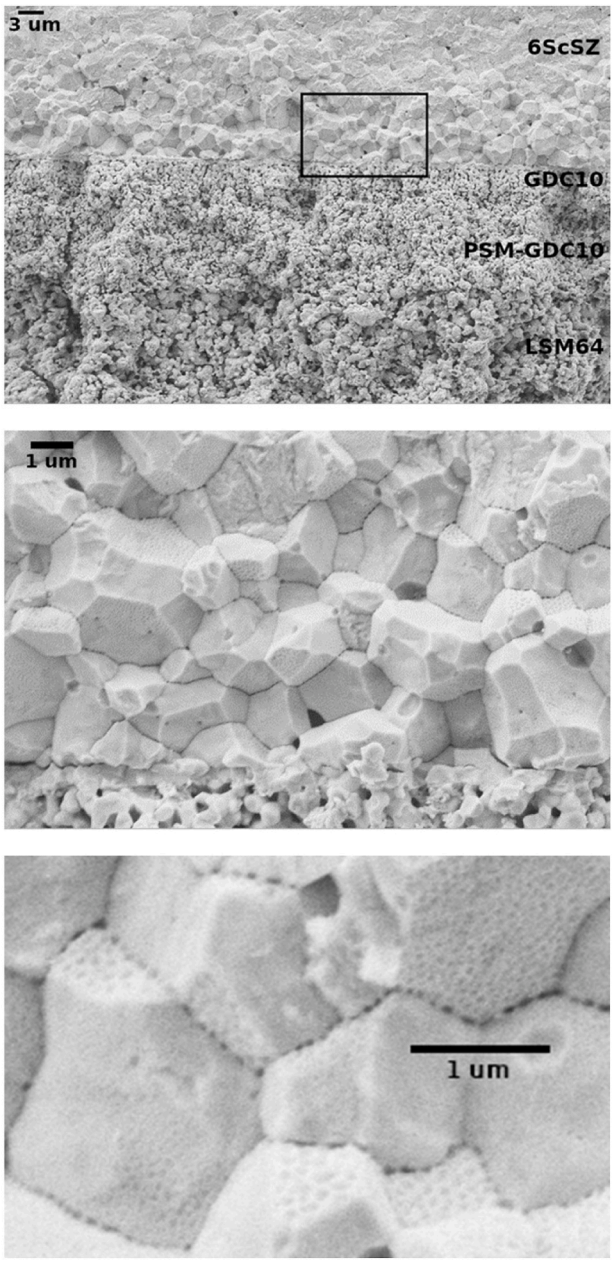


**Fig. 11.** SEM images of a fractured MEA (anode side) after testing in the steam electrolysis regime for approximately 400 h under the current loads of 10–45 A. The area marked by rectangle in (A) is shown in (B) at higher magnification; (C) shows a part of (B).

$cm^2$ and active electrode area of $9 \times 9$ $cm^2$ were produced, assembled in a short stack and tested in the steam electrolysis mode at 1123 K. Water vapor was delivered into the cathode chamber using hydrogen as a carrier gas. The hydrogen production rate, faradaic efficiency and specific energy consumption were determined as functions of the applied current. These values were compared for a hermetically sealed reference stack and a stack after partial unhermetization. Unlike the hermetic systems, the energy conversion efficiency in the partly unhermetized SOEC stack exhibits a drastic increase with increasing applied current. The energy consumption in this stack decreases with increasing current until the onset of solid electrolyte degradation. An appropriate operation regime in the presence of physical leakages was achieved at the current density of 346 mA/$cm^2$ and voltage below the thermal neutral one. Higher currents induce microstructural degradation of the solid electrolyte ceramics and resultant increase in the ohmic resistance. An acceptable energy consumption necessary for the generation of 1 $Nm^3$ of hydrogen was estimated as ~3 kWh. No delamination of $(Pr_{0.6}Sr_{0.4})_{0.97}MnO_{3-\delta}$ based air electrode under steam electrolysis conditions was detected.

## CRediT authorship contribution statement

**E.V. Tsipis:** Writing – review & editing, Writing – original draft, Validation, Methodology. **A.V. Samoilov:** Investigation, Formal analysis, Data curation. **D.V. Matveev:** Investigation, Formal analysis, Data curation. **Yu.S.Fedotov:** Investigation, Formal analysis, Data curation. **M.S. Dyakina:** Investigation. **D.V. Zhigacheva:** Data curation. **D.A. Agarkov:** Writing – review & editing, Writing – original draft, Resources, Funding acquisition. **S.I. Bredikhin:** Resources, Methodology, Funding acquisition, Conceptualization. **V.V. Kharton:** Writing – review & editing, Writing – original draft, Methodology, Conceptualization.

## Declaration of competing interest

The authors declare that they have no known competing financial interests or personal relationships that could have appeared to influence the work reported in this paper.

## Acknowledgments

This work was supported by the Russian Science Foundation (grant 20-19-00478).

## References

[1] Bui T, Lee D, Ahn KY, Kim YS. Techno-economic analysis of high-power solid oxide electrolysis cell system. Energy Convers Manag 2023;278:116704. https://doi.org/10.1016/j.enconman.2023.116704.
[2] Arsad AZ, Hannan MA, Al-Shetwi AQ, Begum RA, Hossain MJ, Ker PJ, Mahlia TMI. Hydrogen electrolyser technologies and their modelling for sustainable energy production: a comprehensive review and suggestions. Int J Hydrogen Energy 2023;48(72):27841. https://doi.org/10.1016/j.ijhydene.2023.04.014.
[3] Abe JO, Popoola API, Ajenifuja E, Popoola OM. Hydrogen energy, economy and storage: review and recommendation. Int J Hydrogen Energy 2019;44(29):15072. https://doi.org/10.1016/j.ijhydene.2019.04.068.
[4] Darda S, Papalas T, Zabaniotou A. Biofuels journey in Europe: currently the way to low carbon economy sustainability is still a challenge. J Clean Prod 2019;208:575. https://doi.org/10.1016/j.jclepro.2018.10.147.
[5] Franchi G, Capocelli M, De Falco M, Piemonte V, Barba D. Hydrogen production via steam reforming: a critical analysis of MR and RMM technologies. Membranes 2020;10(1):10. https://doi.org/10.3390/membranes10010010.
[6] Kayfeci M, Keçebaş A, Bayat M. Chapter 3 – hydrogen production. In: Calise F, D'Accadia MD, Santarelli M, Lanzini A, Ferrero D, editors. Solar hydrogen production. Academic Press; 2019. p. 45–83.
[7] Singh R, Dutta S. A review on $H_2$ production through photocatalytic reactions using $TiO_2$/$TiO_2$-assisted catalysts. Fuel 2018;220:607. https://doi.org/10.1016/j.fuel.2018.02.068.
[8] Quandt KH, Streicher R. Concept and design of a 3.5 MW pilot plant for high temperature electrolysis of water vapor. Int J Hydrogen Energy 1986;11(5):309. https://doi.org/10.1016/0360-3199(86)90149-7.
[9] Hauch A, Küngas R, Blennow P, Hansen AB, Hansen JB, Mathiesen BV, Mogensen MB. Recent advances in solid oxide cell technology for electrolysis. Science 2020;370(6513):eaba6118. https://doi.org/10.1126/science.aba6118.
[10] Stempien JP, Ding OL, Sun Q, Chan SH. Energy and exergy analysis of Solid Oxide Electrolyser Cell (SOEC) working as a $CO_2$ mitigation device. Int J Hydrogen Energy 2012;37(19):14518. https://doi.org/10.1016/j.ijhydene.2012.07.065.
[11] Technical Specifications HOGEN® S Series Hydrogen Generation Systems, https://www.gastech.co.il/images/generators/S-Series/200265-105Nmh_Proton/20Tech/20Specs_RevC.pdf.
[12] Electrolysis station EL 2.1 https://handbook.enapter.com/electrolyser/el21/downloads/Enapter_Datasheet_EL21_RU.pdf.
[13] Carmo M, Flitz DL, Mergel J, Stolten D. A comprehensive review on PEM water electrolysis. Int J Hydrogen Energy 2013;38(12):4901. https://doi.org/10.1016/j.ijhydene.2013.01.151.
[14] Nechache A, Hody S. Alternative and innovative solid oxide electrolysis cell materials: a short review. Renew Sustain Energy Rev 2021;149:111322. https://doi.org/10.1016/j.rser.2021.111322.
[15] Dannesboe C, Hansen JB, Johannsen I. Catalytic methanation of CO2 in biogas: experimental results from a reactor at full scale. React Chem Eng 2020;5:183. https://doi.org/10.1039/C9RE00351G.

[16] Posdziech O, Schwarze K, Brabandt J. Efficient hydrogen production for industry and electricity storage via high-temperature electrolysis. Int J Hydrogen Energy 2019;44(35):19089. https://doi.org/10.1016/j.ijhydene.2018.05.169.
[17] Küngas R, Blennow P, Heiredal-Clausen T, Nørby TH, Rass-Hansen J, Hansen JB, Moses PG. Progress in SOEC development activities at haldor Topsøe. ECS Trans 2019;91(1):215. https://doi.org/10.1149/09101.0215ecst.
[18] Königshofer B, Höber M, Nusev G, Boškoski P, Hochenauer Ch, Subotić V. Accelerated degradation for solid oxide electrolysers: analysis and prediction of performance for varying operating environments. J Power Sources 2022;523: 230982. https://doi.org/10.1016/j.jpowsour.2022.230982.
[19] Sohal MS, O'Brien JE, Stoots CM, SharmaVI Yildiz B, Virkar A. Degradation issues in solid oxide cells during high temperature electrolysis. J Fuel Cell Sci Technol 2012;9(1):011017. https://doi.org/10.1115/1.4003787.
[20] Tsipis EV, Matveev DV, Sharafutdinov AU, Yalovenko DV, Samoilov AV, YuS Fedotov, Dyakina MS, Zhigacheva DV, Agarkov DA, Bredikhin SI, Kharton VV. Performance of SOFCs using model waste gases: a case study. Fuel 2024;358: 130129. https://doi.org/10.1016/j.fuel.2023.130129.
[21] Tsipis EV, Sharafutdinov AU, Matveev DV, Dyakina MS, Zhigacheva DV, Yalovenko DV, Paduchev AP, Bredikhin SI, Kharton VV. Utilization of coal mine gas in solid oxide fuel cells: a performance evaluation. J Power Sources 2024;591: 233834. https://doi.org/10.1016/j.jpowsour.2023.233834.
[22] Agarkova EA, Matveev DV, Fedotov YS, Ivanov AI, Agarkov DA, Bredikhin SI. Processing of manganite-based contact layers for stacking of planar solid oxide fuel cells. Mater Lett 2022;309:131462. https://doi.org/10.1016/j.matlet.2021.131462.
[23] Samoilov AV, Agarkov DA, Fedotov YS, Bredikhin SI. Internal conversion in the membrane-supported SOFC. ECS Trans 2021;103(1):211. https://doi.org/10.1149/10301.0211ecst.
[24] Jin X, Huang K. Precautions of using three-electrode configuration to measure electrode overpotential in solid oxide electrochemical cells: insights from finite element modeling. J Electrochem Soc 2020;167:124501. https://doi.org/10.1149/1945-7111/aba876.
[25] Chan S, Chen X, Khor K. Reliability and accuracy of measured overpotential in a three-electrode fuel cell system. J Appl Electrochem 2001;31:1163–70. https://doi.org/10.1023/A:1012232301349.
[26] Kharton VV, Tsipis EV. Reference electrodes for solid electrolyte devices. In: Inzelt G, Lewenstam A, Scholz F, editors. Handbook of reference electrodes. Berlin-Heidelberg: Springer-Verlag; 2013. p. 243–78. ISBN: 978-3-642-36187-6.
[27] Primdahl S, Mogensen M. Gas conversion impedance: SOFC anodes in $H_2/H_2O$ atmospheres. ECS Proc 1997;1997–40:530–9. https://doi.org/10.1149/199740.0530PV.
[28] Taubmann J, Sun X, Rizvandi OB, Frandsen HL. Advanced insights into gas conversion and diffusion impedance of solid oxide cells by 2D multi-physics modelling. J Power Sources 2023;588:233739. https://doi.org/10.1016/j.jpowsour.2023.233739.
[29] Park B-K, Zhang Q, Voorhees PW, Barnett S. Conditions for stable operation of solid oxide electrolysis cells: oxygen electrode effects. Energy Environ Sci 2019;12:3053. https://doi.org/10.1039/C9EE01664C.
[30] Knibbe R, Traulsen ML, Hauch A, Ebbesen SD, Mogensen M. Solid oxide electrolysis cells: degradation at high current densities. J Electrochem Soc 2010; 157:B1209. https://doi.org/10.1149/1.3447752.
[31] Tietz F, Sebold D, Brisse A, Schefold J. Degradation phenomena in a solid oxide electrolysis cell after 9000 h of operation. J Power Sources 2013;223:129. https://doi.org/10.1016/j.jpowsour.2012.09.061.
[32] Kim J, Ji H-I, Dasari HP, Shin D, Song H, Lee J-H, Kim B-K, J H-J, Lee H-W, Yoon KJ. Degradation mechanism of electrolyte and air electrode in solid oxide electrolysis cells operating at high polarization. Int J Hydrogen Energy 2013;38(3): 1225–35. https://doi.org/10.1016/j.ijhydene.2012.10.113.